Journal of Micromechanics and Microengineering

Semi-reflective visor-based compact head-worn light field display

OPEN ACCESS
IOP Publishing
Journal of Micromechanics and Microengineering
J. Micromech. Microeng. **33** (2023) 055006 (10pp)
https://doi.org/10.1088/1361-6439/acc955

Semi-reflective visor-based compact head-worn light field display

Hongbae Park[1,*] **and Boris Stoeber**[1,2]

[1] Department of Electrical and Computer Engineering, The University of British Columbia, Vancouver, BC, Canada
[2] Department of Mechanical Engineering, The University of British Columbia, Vancouver, BC, Canada

E-mail: hongbae@ece.ubc.ca

Received 28 November 2022, revised 23 March 2023
Accepted for publication 31 March 2023
Published 11 April 2023

Abstract

We propose a visor-based see-through head-worn light field display. The visor is a semi-reflective concave image combiner that overlays virtual imagery to the user's visual field. The visor has a toroidal surface profile for off-axis astigmatism correction. Virtual images are created at different depths using a classical light field assembly (LFA), which comprises a microlens array and a display source. The LFA is placed at an angle above the visor, clear of the user's line of sight. The image plane of the LFA is placed near the focal plane of the visor. Since the LFA forms virtual images farther away from the plane of the display source, the LFA itself can be brought close to the visor, allowing for a more compact display system compared to conventional head-worn displays.

Keywords: light field, near-eye display, microlens array

(Some figures may appear in colour only in the online journal)

1. Introduction

Amongst the divergent optical designs for head-worn displays (HWDs), designs that incorporate semi-transparent reflectors as the combiner have been the earliest types of head-mounted displays [1–3]. These designs are sometimes referred to as the bug-eye system, due to the resemblance of the globular combiner shape to insect eyes. Despite the advances in the design of HWDs that use diffractive, holographic, microstructured, and/or freeform optics [4–9], the reflector-based designs have proliferated thanks in part to the relative simplicity in constructing a combiner out of a semi-reflective surface. This approach also allows for a large field of view (FOV) and a large eyebox, while accommodating glasses-wearers. As such they are found in a wide variety of applications, from military applications such as pilot helmets [10, 11] to consumer applications such as augmented reality headsets [12–14]. Some of the recent developments in reflector-based designs make use of deformable reflectors [15, 16] or foveated imaging technique [17]. One considerable drawback, however, is that reflector-based systems tend to be bulky, which gives them poor aesthetics. Another set of recent works describes smaller form-factor systems using folded optics designs [18, 19], however, at the cost of the FOV.

This work demonstrates a new configuration of head-worn light field displays (LFDs) that use a visor-type image combiner. In general, LFDs are displays capable of generating images at varying depths from the eye, by emulating the light field emanating from a volumetric scene. The advantages are largely two-fold; first, the virtual image-forming light field assembly (LFA) can be placed much closer to the combiner than the intrinsic focal plane of the image combiner. This can reduce the headset size and allows the device to sit closer to the face compared to conventional designs, which are essential characteristics for building a smaller form-factor device

* Author to whom any correspondence should be addressed.

compared to existing reflector-based HWDs [12–17]. Second, the pitches of the elemental image and the microlens array (MLA) are equal in our LFA, which makes our LF-HWD a telecentric system, i.e. the FOV is constant over the depth range with no vignetting at the peripheries of the virtual image. This allows us to make the LFA behave like a pupil expander that produces divergent beams, with a minimal amount of pixel redundancy between elemental images. An elemental image is a section of a scene containing the light field corresponding to the section being viewed from a certain perspective and position. These characteristics in turn enlarge the eyebox and increase the effective resolution of the virtual light field image. This is an advantage over traditional LFDs that do not use a combiner [20] and previous reflector-based integral imaging display [21] that must deal with a trade-off between the eyebox size and the effective resolution. As well, using a semi-transparent combiner does not deteriorate the see-through imagery unlike in direct-view type LFDs [22, 23] where the display and microstructure arrays are placed in the user's line of sight. In the following sections, we describe in detail the imaging principle of the proposed display system and simulation results, as well as the implementation of the proposed system through a prototype and the characterization of that prototype.

2. Laying the groundwork

2.1. Theory

The proposed display system is composed mainly of two optical components, the concave reflector and the LFA, which is an assembly of a MLA and a display panel. Figure 1 depicts the side-view of the system. The concave reflector is tilted upwards at an angle θ_{rt} in the yz-plane with respect to the line of sight of the user, and the LFA plane is tilted by $2\theta_{\mathrm{rt}}$.

Figure 2 shows the LFA and the ray propagation through it in closer detail. The LFA is in a Galilean configuration [8, 24], which forms a virtual image on the opposite side of the MLA, rather than a real image between the reflector and the LFA. The virtual image plane of the LFA is placed at the focal plane of the reflector such that it introduces telecentricity. The reflector forms the final virtual image that is perceived by the user. In figure 2, the three green squares represent light-emitting pixels on the display panel, each in one of the three neighboring elemental images, that collectively form a single point image in the virtual image plane of the LFA. The point image is formed along the refracted rays passing through the microlenses, that emanate from these pixels. The angle of incidence

$$\delta_{\mathrm{i}} = \tan^{-1}\left(\frac{Np_{\mathrm{p}}w_{\mathrm{shift}}}{d}\right) \approx \frac{Np_{\mathrm{p}}w_{\mathrm{shift}}}{d} \tag{1}$$

of the chief ray shown in figure 2 is related to the MLA thickness d (assuming a negligible microlens sag), and the shift distance between adjacent elemental images w_{shift} (in number of pixels). The additional variables p_{p} and N in equation (1) represent the pixel pitch and an integer denoting the Nth position

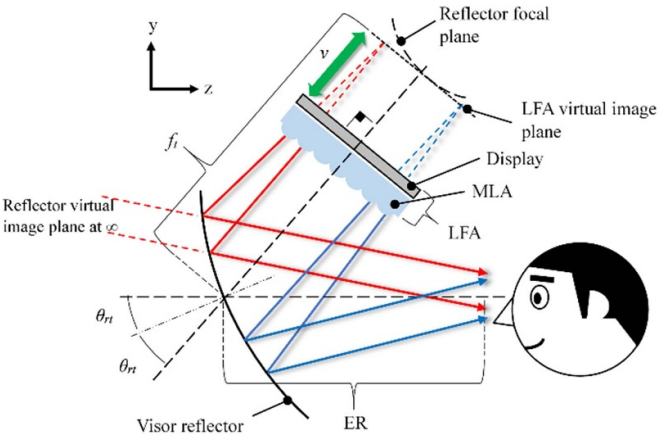

Figure 1. Side-view of the reflector-based LFD.

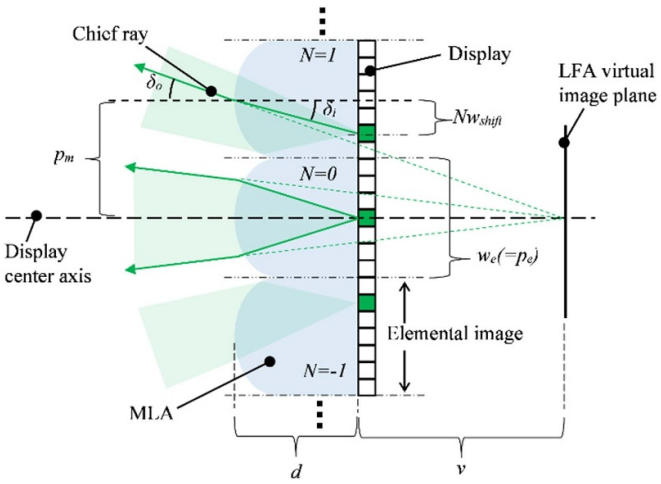

Figure 2. Ray propagation and virtual image formation of the LFA. In this example, $w_{\mathrm{e}} = p_{\mathrm{e}}$. We assume the display panel is infinitesimally thin. The gaps between the three beam paths are assumed negligible with 100% fill factor MLA.

of the microlens and the elemental image pair from the center axis of the display (the on-axis position being the 0th position of the array). This yields the angle of refraction of the chief ray

$$\delta_{\mathrm{o}} = \sin^{-1}\left[n\sin\left(\delta_i\right)\right] \approx n\delta_{\mathrm{i}}, \tag{2}$$

where n is the refractive index of the MLA. Equations (1) and (2) are true, provided a paraxial condition in which $p_{\mathrm{p}}w_{\mathrm{shift}}/d$ is small. In the same paraxial condition, the LFA virtual image distance (as shown in figure 2)

$$v \approx \frac{dp_{\mathrm{m}}}{np_{\mathrm{p}}w_{\mathrm{shift}}} - d, \tag{3}$$

measured from the display plane (assuming negligible display thickness) depends on the additional variable p_{m}, the microlens pitch.

Evidently from equation (3), we can create multiple image planes as v varies with the change in w_{shift}. In order for the

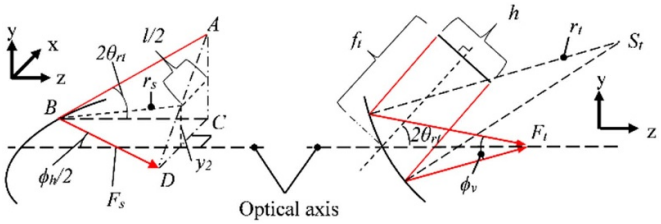

Figure 3. Left: horizontal FOV formation in the *xz*-plane. *A* is a point on the LFA's virtual image plane. Points *B, C*, and *D* lie on the *xz*-plane. Right: in the tangential (vertical) *yz*-plane. S_t represent the reflector's center of curvature in the tangential plane.

reflector to form a virtual image over the entire range of v produced by the LFA, the plane of the farthest possible v (using the lowest possible w_{shift}) needs to be placed at the focal plane of the reflector. As a result, for the plane of the farthest v, the final virtual image formed by the reflector is at optical infinity; increasing w_{shift} brings the virtual image closer to the user. Because the reflector is tilted with respect to the LFA, a significant amount of oblique astigmatism is introduced. As such, we use a simple toroidal reflector, having different spherical radii r_s and r_t in the sagittal and tangential planes, respectively, to correct for the off-axis reflection [25]. Such a reflector can readily be fabricated in-house using a 3D printing-based process (section 3.1). It is worth noting that the telecentric configuration of the system allows us to set p_m equal to the elemental image pitch p_e (or w_e if $w_e = p_e$, both variables are in number of pixels), unlike in direct-view and reflector-based LFDs [20, 21] where these quantities are typically dissimilar. This enforces here a coaxial and identical optical relationship between each pair of microlens and its corresponding elemental image over the entire LFA, which helps to maintain a uniform FOV over the virtual image depth field, and imaging condition such as brightness across the virtual image.

Figure 3 shows the ray propagation and key parameters for estimating the horizontal and vertical FOV. The horizontal FOV ϕ_h can be estimated such that

$$\phi_h = 2\tan^{-1}\left(\frac{\overline{CD}}{\overline{BC}}\right), \tag{4}$$

where

$$\overline{BC} \approx \sqrt{{r_s}^2 + \left(\frac{l}{2}\right)^2}\cos(\theta_{rt}), \tag{5}$$

$$\overline{CD} = \frac{l}{2}\frac{\overline{AC}}{\overline{AC} - y_2}. \tag{6}$$

In equations (5) and (6), l is the width of the lightfield image on the display, and

$$y_2 = \overline{BC}\tan(\theta_{rt}). \tag{7}$$

The vertical FOV approximated as

$$\phi_v \approx 2\tan^{-1}\left[\frac{h}{r_t\cos(\theta_{rt})}\right]. \tag{8}$$

Note that we assume both tangential and sagittal contours of the reflector are spherical. As well, we assume the convergence point F_t (figure 3 right) is on-axis for convenience. The effective pixel resolution

$$\text{ER} = w_{\text{shift}}(N_{\text{max}} - 1) + w_e \tag{9}$$

of the virtual image (also of the original image before light field conversion) is given in number of pixels. In equation (9), N_{max} is the total number of elemental images in 1D, which is also equal to the display pixel resolution divided by w_e. It should be emphasized that ER is a function of w_{shift}, which suggests that the apparent size of the virtual image will differ at different depths. In other words, when the original image of a fixed pixel resolution (fixed size) is sampled with different w_{shift} values for creating a virtual image at different depths, N_{max} changes (**increasing** w_{shift} **decreases** N_{max}). Since N_{max} is directly proportional to the LFA width and height l and h, the virtual image size in terms of the FOV will **decrease** when w_{shift} **increases** (virtual image at nearer distance), and vice versa.

The size of the eyebox

$$\text{Eyebox} = \text{floor}\left(\frac{w_e}{w_{\text{shift}}}\right) \times \frac{p_m f_t}{(d+v)} \tag{10}$$

assumes 100% microlens fill-factor. Contrary to the traditional MLA-based LF-HWD such as [18] and [20], whose eyebox size is close to floor $(w_e/w_{\text{shift}}) \times p_m$, the use of the reflector introduces the multiplier term $f_t/(d+v)$ to the eyebox size equation. A tangible interpretation of this term is that the width of the beam as it departs the MLA (figure 2), will have expanded by the multiplier term when it reaches the reflector, since it is diverging. With $f_t/(d+v) > 1$, we can use a larger value for w_{shift}, which increases the effective resolution according to equation (9). Note that the dependence of the eyebox size on floor (w_e/w_{shift}) suggests that the virtual images at different depths will have different eyebox sizes. Also, it should be noted that the ray convergence points F_s and F_t (figure 3) in the sagittal and the tangential plane, respectively, may not be identical depending on the curvature of the reflector in the respective planes.

2.2. Simulation

We use raytracing software Zemax OpticStudio to validate the imaging theory outlined in section 2.1. Figure 4 shows the simulation setup in the non-sequential mode in OpticStudio.

The setup consists of an LFA, a toroidal reflector, and an ideal eye to bring the reflector image into focus. Table 1 lists the parameters used in the simulation. Note that some parameters are fixed quantities. Other parameters are determined arbitrarily but influenced by the fixed parameters, MLA fabrication constraints, and consideration for the eyebox size. For example, p_m is chosen as such because it must be an integer multiple of p_p and is also close to the maximum microlens base diameter we can reliably fabricate. A larger microlens is desired as it increases the eyebox size. Since the eyebox size can also vary depending on the value of w_{shift} as per

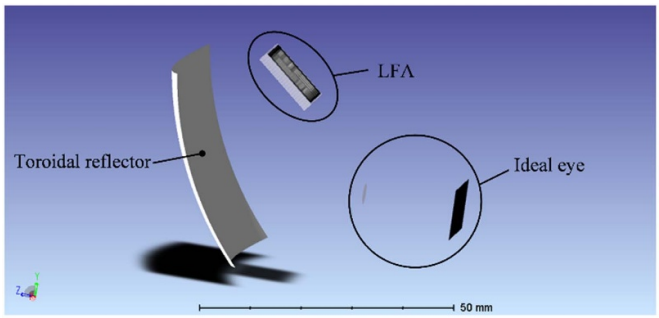

Figure 4. Visualization of the simulation setup in OpticStudio.

Table 1. Simulation parameters and their values.

Parameter (description)	Value
d (microlens thickness, including microlens sag height)	2 mm
f_t (distance to tangential focal plane from reflector center)	25.8 mm
h (maximum display image height)	19.584 mm
l (maximum display image width)	29.376 mm
n (refractive index of the MLA (material: PDMS))	∼1.43
p_m (microlens pitch)	612 μm
p_p (pixel pitch)	36 μm
r_s (sagittal radius of curvature of the toroidal reflector)	57.5 mm
r_t (tangential radius of curvature of the toroidal reflector)	70 mm
v (LFA virtual image depth)	2.76–5.93 mm
w_e (elemental image size in # of pixels)	17
w_{shift} (elemental image shift in # of pixels)	3–5
θ (tilt angle of the reflector)	25°
Distance from ideal eye pupil to retinal detector	19 mm
Ideal eye pupil diameter	4 mm
Ideal eye retinal detector size	8 mm × 8 mm (800 px × 800 px)
Microlens fill factor	100%
Microlens radius of curvature	722 μm

equation (10), the range of w_{shift} is chosen such that the eyebox size remains nearly constant over the depth field. r_t and r_s are chosen under paraxial assumptions such that the center of the LFA virtual image plane is in sharpest focus at the ideal eye retina. The remaining parameters are then set automatically. For example, the microlens radius of curvature (ROC) is chosen as such to collimate the light from the display for a given d and n.

The model constructed using the parameters listed in table 1 has a horizontal and vertical FOV of 48.3° × 34.3° with an eyebox size of ∼10 × 10 mm^2, and the effective resolution of 158 × 110 pixels at the farthest field (virtual image at infinity) and 252 × 172 pixels at the nearest field about 290 mm away

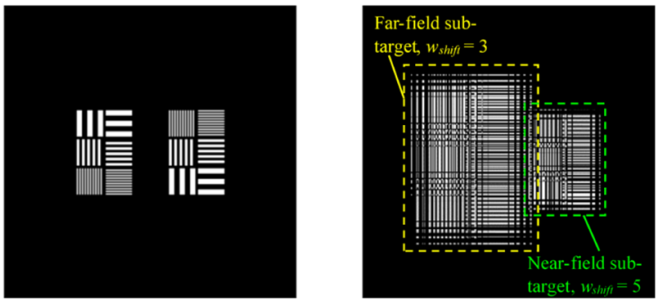

Figure 5. Test image with two sub-targets (2 × 3 pairs of horizontal and vertical B/W line targets at different spatial frequencies), for far and near-field image projection. Left: the original sub-targets before light field conversion. The two side-by-side sub-targets are identical except one is flipped upside down, and they are 42 × 60 px in size. Right: the sub-targets after conversion. Note the different apparent sizes of the line pair targets after conversion, due to different w_{shift} values being used.

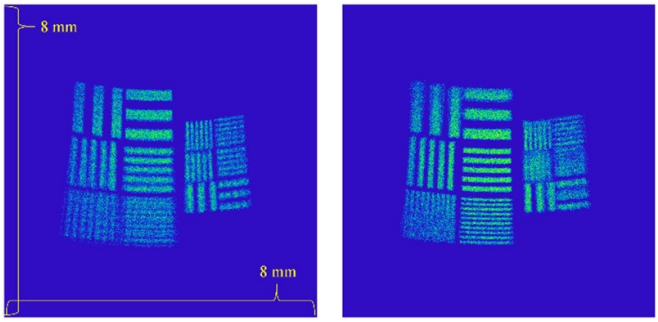

Figure 6. OpticStudio-simulated false color images on the retinal detector with the eye focused at different depths, using the test targets shown in figure 5. Left: eye focused at ∼290 mm (eye focal length = 17.9 mm) from the eye pupil and the right sub-target is in focus. Right: eye focused at infinity (eye focal length = 19 mm) with the left sub-target in focus.

from the eye. The distance between the LFA and the reflector is mostly constrained by the fabrication limitations. Ideally, the LFA should be very close to the visor for a couple of reasons. First, this reduces the form factor as much as possible. Second, it allows for the separation of the LFA virtual image plane from the physical LFA plane to prevent the physical structure of the LFA from being seen when the virtual image is in focus. However, this requires microlenses with a longer focal length (larger ROC), but microlenses with too shallow of a sag are not commercially available and cannot be made using our current fabrication process (to be explained further in section 3.2). As a result, the maximum distance v to the display from the reflector we can achieve is limited to only ∼6 mm, which also limits the size reduction of the prototype.

Figure 5 shows the test image used in the simulation. The test image consists of two adjacent sub-images, each of which has been converted into light field patterns from the test target image on the left side of figure 5, using w_{shift} = 3 and 5. This in turn forms virtual images at different distances from the eye; OpticStudio estimates that the larger left sub-target forms a virtual image at infinity, and the smaller right sub-target at ∼290 mm from the eye pupil. Figure 6 shows the simulated

retinal images on the ideal eye, with the eye focused at near and far-field virtual images.

3. Building the prototype

3.1. Fabrication of the toroidal reflector

A toroidal reflector suited for our design parameters does not appear to be commercially available, so we turn to fabricating our own by thermoforming a polyethylene terephthalate glycol (PETG) sheet over a mold. A similar approach is described in [17]. Unlike [17] however, where the thermoformed plastic is temporarily used as an envelope to help an optical glue cure and smooth the surface, after which it is discarded, we use the thermoformed PETG sheet as the reflector. The mold is printed with an Anicubic Photon stereolithography printer, using their clear resin. The mold is designed in a way that the outer surface of the thermoformed reflector touches the mold. The surface of the mold is manually polished using a 600-grit wet sandpaper, to prevent the thermoformed reflector from taking on the roughness of the 3D-printed mold surface. However, in our experiments, manual polishing (even with higher-grit sandpapers) does not provide an adequate smoothness. As well, excessive polishing can distort the curvature of the mold and leave scratches on the surface. Therefore, after a quick polish, we lightly coat the surface of the mold using an epoxy resin (Max Clear resin from Polymer Composites Inc.). This seals the surface irregularities, resulting in a smoother surface due to surface tension. The curvature of the mold was compensated to account for the thickness of the plastic sheet and the resin coating which combined are about 1 mm. The PETG sheet is then vacuum thermoformed over the mold using a generic thermoformer with a 600 W heating coil. After thermoforming, the inner surface (concave side) of the thermoformed reflector is sputter coated with a 10 nm layer of silver using an Angstrom Engineering PVD sputter coater. The resulting reflectance is about 50%, measured using an Avantes AvaSpec-2048L spectrometer. Figure 7 shows the mold after resin coating and the thermoformed reflector after silver deposition.

3.2. Fabrication of the MLA

The MLA is double-cast from a microfabricated MLA mold on a silicon wafer. Figure 8 shows the final double-cast MLA on a 51 mm × 76 mm glass slide with a 1 mm thickness. For fabrication of the MLA mold, we follow an identical photolithography and reflow process as shown in [26]. First, hexamethyldisilane is vapor-deposited on a 4 inch silicon wafer to promote adhesion between the wafer and the photoresist. Next, a ∼35 μm thick photoresist film (AZ 4620 positive photoresist) is spin-coated using a two-step coating procedure (first layer spin-coated at 730 rpm and second layer at 3000 rpm using a Headway PWM32 spinner), and baked on a hot plate at 100 °C. Then, the photoresist is exposed through a photomask and developed, which results in an array of cylindrical

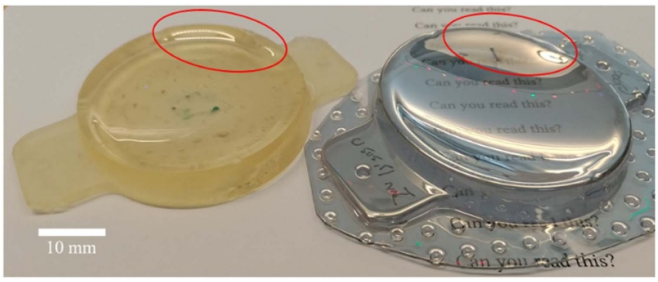

Figure 7. Epoxy-coated thermoforming mold (left) and the thermoformed and silver-deposited reflector. The excess resin did not drain completely and beaded partially at the edge of the mold (red circles). However, this is not critical to the functioning of the reflector. The reflector is semi-transparent as the text underneath is visible. The reflector is about 50 mm in diameter across the short side (sagittal plane) and 55 mm across the long side (tangential plane).

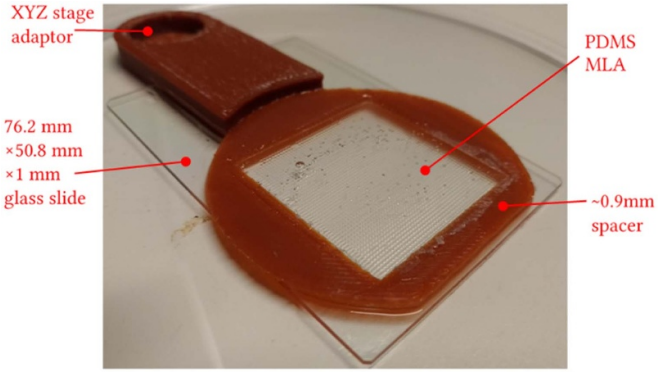

Figure 8. PDMS MLA on a glass slide with 3D printed components attached for mounting on the XYZ positioning stage.

photoresist islands. Finally, the wafer is heated to 145 °C to reflow the photoresist islands, at which point they become spherical caps (or lenses) due to the surface tension of the molten photoresist while maintaining their footprint. If the height of the spherical cap (sag height) is very small compared to the lens diameter, then the photoresist reflow process will require a substantial amount of lateral reflow of highly viscous photoresist to achieve a spherical cap, which can take a long time. This is associated with the risk that the photoresist might be damaged by long exposure to the high reflow temperature. To reduce the risk of photoresist damage, conditions of the reflow e.g. the aspect ratio between the sag height and the lens footprint need to be met. Chapter 4 in [27] includes an in-depth study on considerations for the reflow process.

The photoresist MLA has a 612 μm pitch (equal to $w_e \times p_p$) with individual microlenses having a ∼580 μm base diameter representing a fill-factor of ∼71%, and a 714 ± 25 μm ROC on average (the target ROC is 721.5 μm). The ROC was measured by scanning the surface profile of the microlenses at the four corners of the array using a Dektak XT mechanical profilometer, then fitting the profilometer data with a

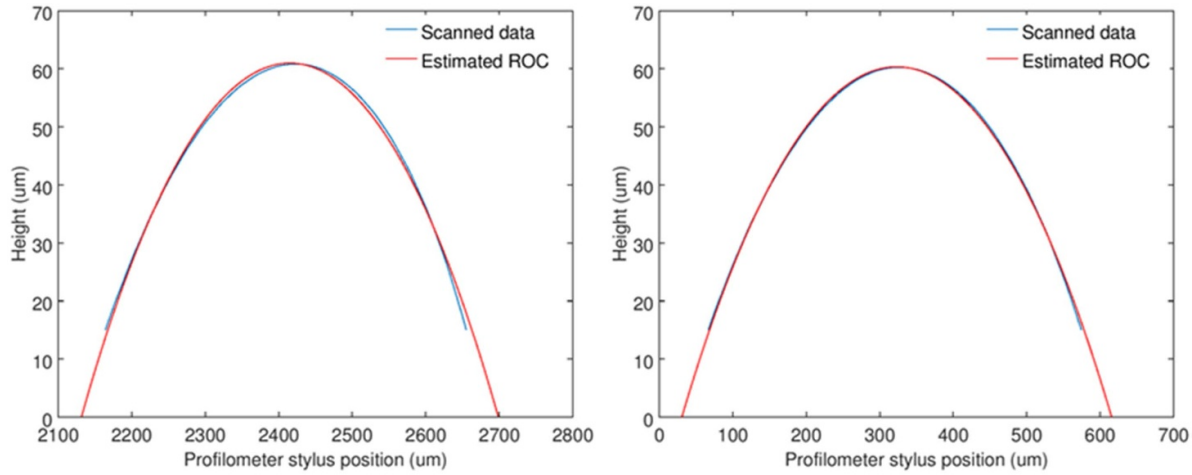

Figure 9. Scanned profile of microlenses and estimated ROC of 690 μm (left) and 738 μm (right). The horizontal and the vertical axes are in different scales.

spherical contour using the Pratt method [28, 29]. The variation in microlens ROC across the array is most likely due to the unevenness in photoresist film thickness after spin coating, which may vary by $\pm 5\%$ for films >8 μm in thickness, according to the manufacturer (Microchemicals GmbH). Figure 9 shows a couple of the scanned microlens profiles with spherical contours fitted to the data. Since the original photoresist MLA on silicon wafer is not visually clear, we use a double-casting process to make a clear replica. We first cast a negative mold of the photoresist MLA using the Max Cast flexible epoxy resin from Polymer Composites Inc. at room temperature for 24 h. Once the negative mold is cured, we cast with PDMS to get the final clear MLA. The PDMS is cured at room temperature for a minimum of 24 h.

3.3. Prototype

We build a prototype using the fabricated reflector and the MLA. Note that this is a monocular system meant to be viewed with one eye. The majority of the other prototype components such as the display frame are 3D printed with a fused deposition modelling (FDM) printer. The MLA is mounted on an XYZ micro-positioning stage (Thorlabs DT12XYZ) for alignment of the MLA with the display. The MLA mount also allows for some rotational freedom in the plane of the MLA. A Sharp LS029B3SX02 LCD panel with a pixel resolution of 1440 $\times$ 1440 pixels, a 36 μm pixel pitch, and a 300 cd m^{-2} of brightness is used as the display source. The 3D-printed display frame rests on a set of threaded nuts, one on each side of the frame, that ride a pair of bolts with a 10–32 thread. Turning the nuts adjusts the distance between the display and the reflector, which is mounted at the ends of the said bolts. The completed prototype assembly is suspended from a retort stand, as shown in figure 10.

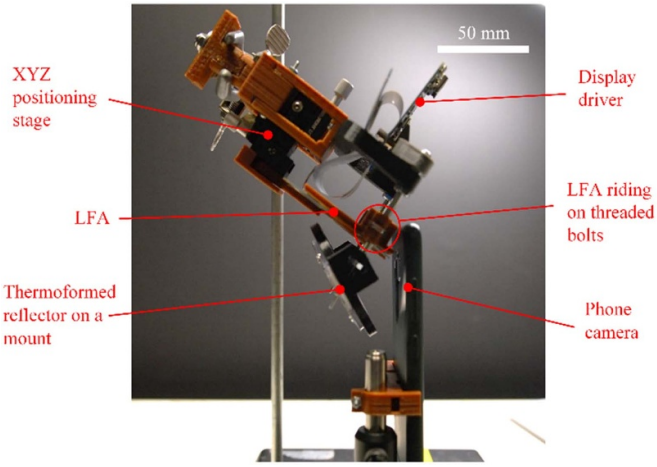

Figure 10. Test setup.

4. Image assessment

We evaluate the optical quality of the toroidal reflector by measuring the modulation transfer function (MTF) from the virtual images of line pair (lp) test targets formed by the toroidal reflector without the LFA in place (figure 11). Note that for this we place the display source at the focal plane of the reflector. We use a Nikon D60 digital camera with a 35 mm lens to capture the virtual images of the test targets in a dark room. The distance between the display and the reflector is adjusted such that the virtual images are formed at as close to optical infinity as possible, with the camera also focused at infinity and pointed at the center of the reflector. Figure 12 shows the comparison between the measured MTF and the OpticStudio estimate using a 4 mm pupil on the ideal eye in both the tangential and the sagittal planes. For the MTF, we measure the relative maximum/minimum luminance per pixel row/column (depending on the direction of the lps), then

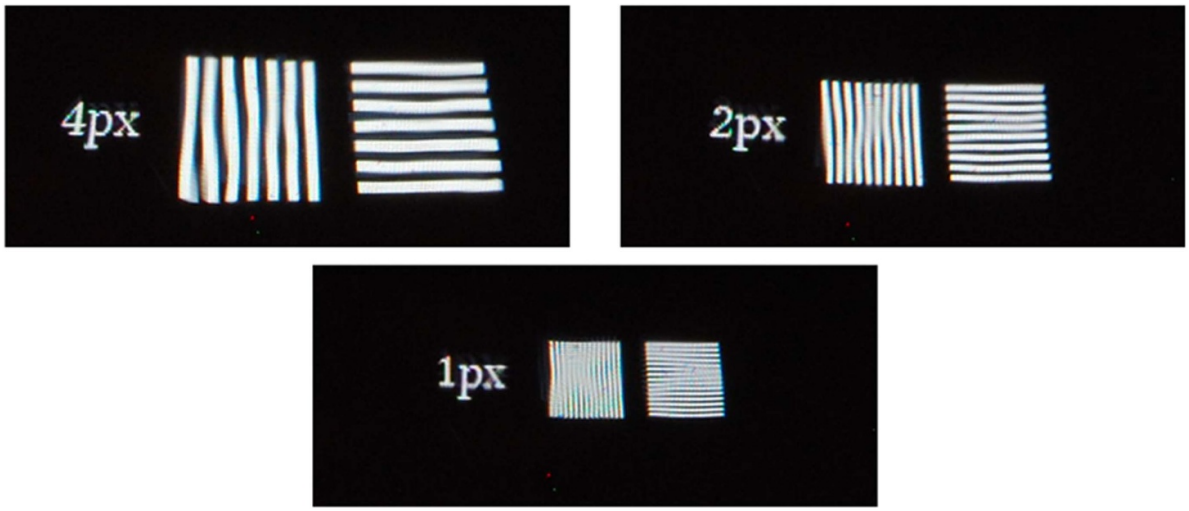

Figure 11. Virtual images of the test targets with varying spatial frequency viewed through the central region of the toroidal reflector. Top left: test target with a 4-pixel line width (3.47 lp mm^{-1}), which spans 6° × 6° FOV horizontally and vertically each. Top right: 2-pixel line width (6.94 lp mm^{-1}), spanning 4° × 4° FOV. Bottom: 1-pixel line width (13.9 lp mm^{-1}), spanning 3° × 3° FOV. The lines of the test targets are warped due to the reflector surface imperfections.

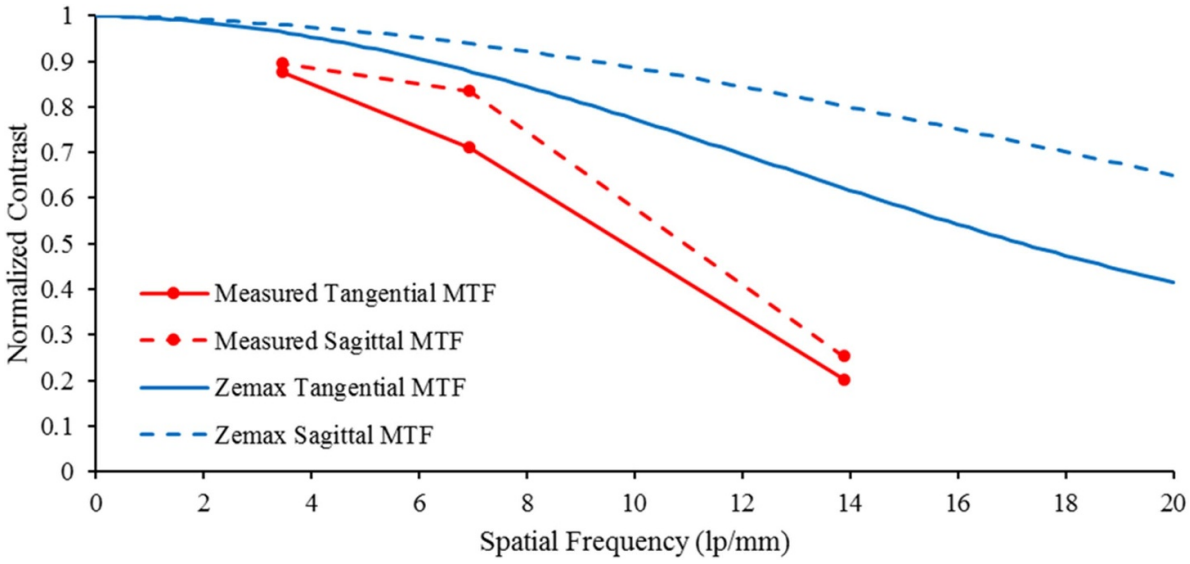

Figure 12. MTF estimated in OpticStudio and the measured MTF.

calculate the contrast and average over the area of the lp targets. Note that the lp targets span about 3° × 3° to 6° × 6°, depending on the spatial frequency, therefore the measured MTF represent an averaged value within these angular ranges. The OpticStudio MTF estimate represents an upper-bound as it was determined using on-axis rays. Regardless, the measured MTF is expected to be lower due to the reflector surface irregularities introduced during fabrication.

We switch to using a LG V40 ThinQ phone camera for capturing the virtual images formed by the light field source images; the Nikon camera with its lens does not fit into the test setup to be positioned close to the reflector within the eye-relief distance. We first measure the FOV by displaying and capturing the image of concentric rings (figure 13), each of which represents a unique angle subtended from the camera. The default LG V40 ThinQ phone camera has a FOV of about 67° × 53° and manual focus adjustability. The measured monocular FOV is approximately 40° × 31°, in line with what is estimated by equations (4)–(8). FOV measurements are also shown in figure 13. Note that this is only about half of the maximum FOV the Sharp display can support (about 73° × 78°, since the display width = height = 51.84 mm). This is because we are limited by the size of the MLA used, which is less than 30 mm × 30 mm.

Figure 14 shows the virtual images we obtain from the test setup through the semi-transparent reflector, using the lp test target shown in figure 5. Because the fabricated MLAs have a fill-factor of ∼70%, stray light that propagates through the gaps between the microlenses causes glare and reduces the quality of the virtual images. To solve this, we implement a

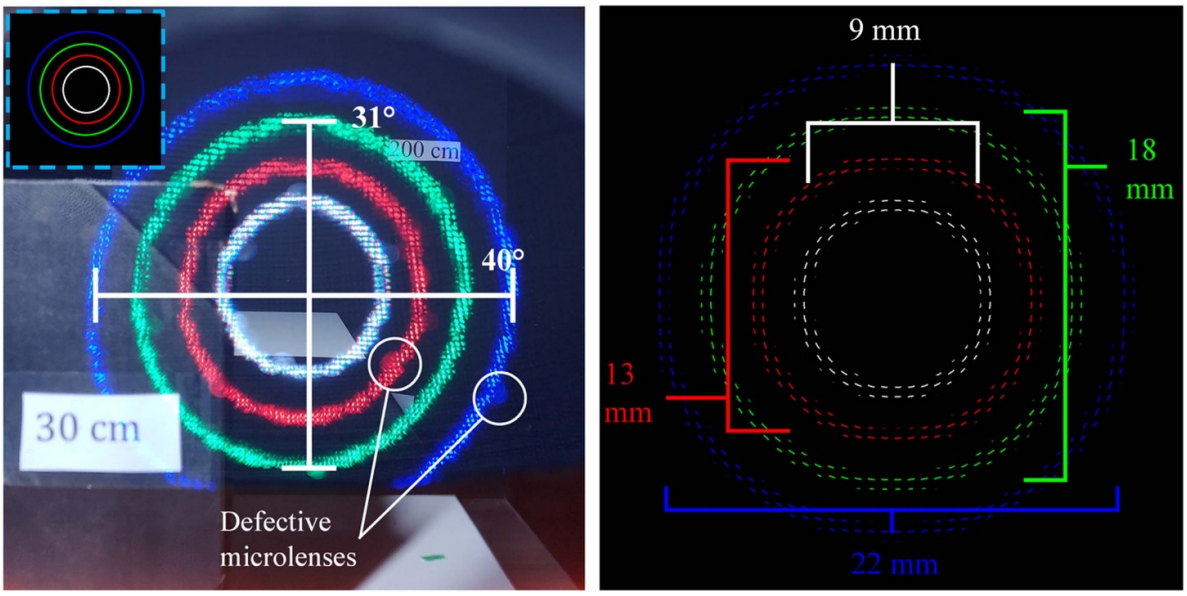

Figure 13. Left: virtual image of the concentric rings for FOV measurement seen through the reflector. Camera focused at infinity. Left: the virtual images of the rings are projected at infinity using $w_{\text{shift}} = 3$. The lengths represent the approximate diameter of the rings ($l = h$) of each ring on the Sharp LS029B3SX02 LCD display. Some defective microlenses are visible (indicated by white circles) as they are illuminated by the display image. The inset image wrapped in the dashed cyan line is the original image used for FOV measurements, prior to being converted into a light field image. Right: light field-converted FOV measurement image.

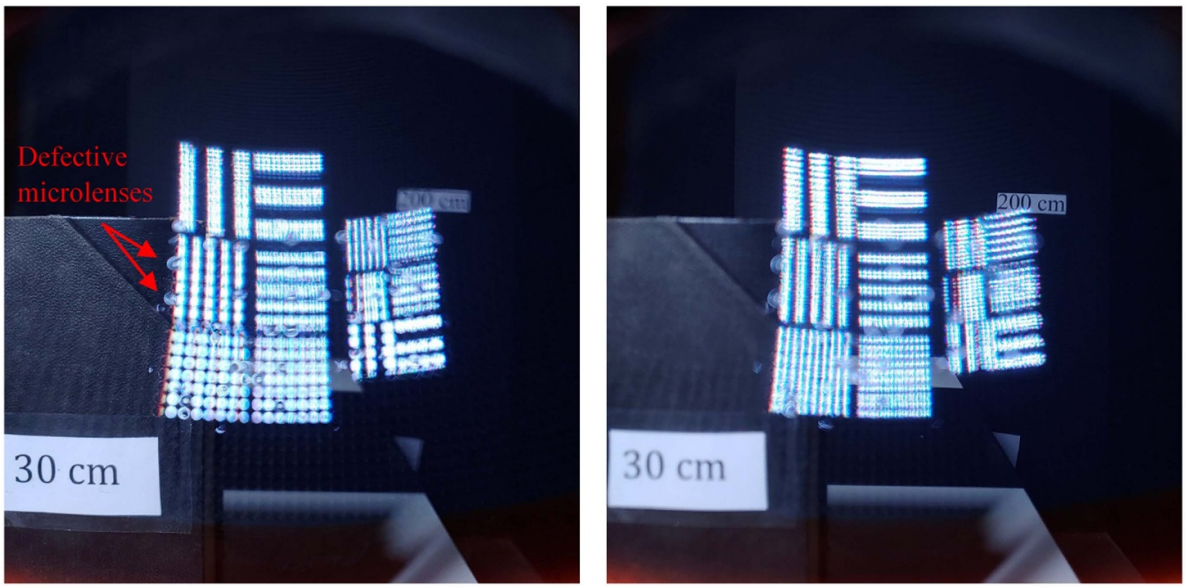

Figure 14. Virtual image of the test targets shown in figure 5 seen through the reflector. Left: virtual image with the camera focused at ∼30 cm. The right sub-test target is in focus with the smallest frequency line pairs on the right resolved. Right: camera focused at infinity (∼200 cm) with the smallest frequency line pairs on the left resolved. Some speckles are visible here and there within the images, which are defective microlenses themselves.

virtual aperture array with the elemental images where each elemental image is formed into a circle with a diameter equal to or smaller than the base diameter of the microlenses, similar to a method introduced in [23]. However, constricting the aperture diameter too much reduces the brightness of the virtual image. We have experimented with different aperture diameters and found that setting the aperture diameter to about 60% of the microlens diameter of 580 μm produces virtual images with a good balance between image quality and brightness. Figure 15(a) shows a test target consisting of two letter sequences, one in green and one in red. The light field-converted test target in figure 15(b) is prepared such that the two letter sequences will appear at different distances in the virtual image. The difference in image quality with and without the virtual aperture array can be observed in figures 15(d)–(f). Figures 15(d) and (e) are camera-captured

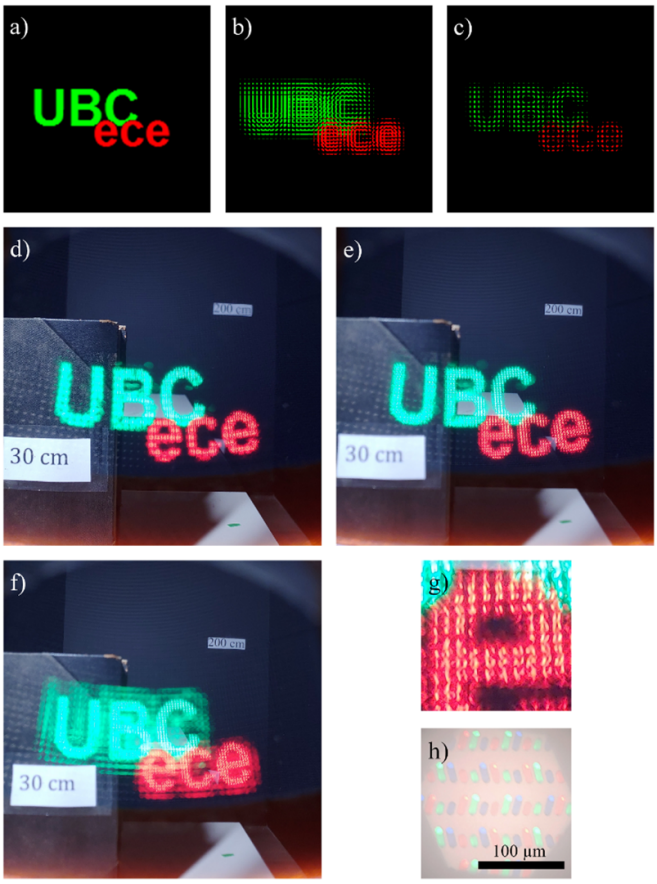

Figure 15. Test image with a simple test target. From the top: (a) the original test target (what the virtual image should look like). (b) Light field-converted test target, no virtual aperture array implemented. Elemental images are square. (c) Light field-converted test target, with a virtual aperture array. Elemental images are roughly circular with a diameter of ∼367 μm (∼63% of the microlens diameter). (d) Looking at the virtual image through the reflector, camera focused ∼30 cm away. The virtual image is generated from the elemental image (c), with a virtual aperture array. The letters 'ece' are in focus. (e) Looking at the same virtual image with the camera focused at infinity (∼200 cm). The letters 'UBC' are in focus. The depth between the two groups of letters is greater than 1.7 m. (f) Virtual image is generated from elemental image (b), without a virtual aperture array. The stray light causes a haze around the main image. (g) Magnified view of the letter 'e' in (e). The red subpixels are visible. (h) Looking at the Sharp display under a microscope. The pixel structures are visible.

virtual images obtained using the elemental image shown in figure 15(c) with the integrated virtual aperture array. Figure 15(f) is a captured virtual image using the elemental image of figure 15(b), without the virtual aperture array.

We identify a few shortcomings in the quality of the virtual images seen through the reflector. First, the virtual images appear grainy and 'squiggly,' as observed in figures 15(d) and (e). This is because the pixel density of the Sharp IPS panel is somewhat low, and the pixels are arranged in a zig-zag pattern, with each pixel being rather large at 36 μm in comparison to the microlenses. In addition, the microlenses magnify the pixel structure and make them more visible, as seen in figures 15(g) and (h). This can be mitigated by using a display with smaller pixels and/or using an intermediate diffusing layer between the MLA and the display. Second, when we shift the camera focus to near field, the MLA structures become visible, as in the left side of figure 14, because the distance at which the MLA structures are imaged by the reflector becomes close to the near field image. This can be remedied by using a higher fill-factor (ideally 100%) MLA such that the amount of stray light is reduced, thereby reducing the chances of the MLA being illuminated due to interreflection within the MLA. Also, moving the LFA closer to the reflector (with a longer MLA focal length), away from the intrinsic focal plane of the reflector, and potentially applying an anti-reflective coating to the MLA may help. Third, defective microlenses in the MLA make the virtual images look as if there are water droplets on them, as in figures 13 and 14. Other aberrations such as distortion are also visible, which should be addressed using a free-form reflector with a non-symmetrical and higher order surface profile, optimizing the microlenses by customizing the microlens focal lengths specific to the microlens location in the array [30], and image pre-processing techniques [31].

5. Conclusions

We present an LFHWD using a semi-transparent toroidal reflector as the image combiner. We show that putting the LFA in a Galilean configuration can reduce the overall size of a visor reflector-based LFHWDs and synchronizing the period of the elemental images to the MLA pitch makes for a telecentric system such that the light field image FOV is constant over the focal depth range. We evaluate the optical quality of the house-made toroidal mirror by measuring the MTF using lp test targets. The MTF measurements, while lower than the MTF estimated in OpticStudio, have expected values given the quality of the mirror. With the prototype assembly we show virtual images generated from light field source images, at different focal planes, captured using a camera. A few shortcomings are identified with the quality of the virtual images seen through the reflector, due to the low quality of the house-fabricated MLA and the characteristics of the display panel used in the prototype, such as the stray light propagating in between the microlenses due to the low fill factor. Despite this, this work demonstrates the capabilities of our new LFHWD concept through a proof-of-principle prototype.

Data availability statement

All data that support the findings of this study are included within the article (and any supplementary files).

Acknowledgments

This research was undertaken, in part, with support from the Canada Research Chairs program.

Funding

Canada Research Chairs (CRC) (950-231712)

ORCID iD

Hongbae Park https://orcid.org/0000-0002-3092-412X

References

[1] Krevelen R V and Poelman R 2010 A survey of augmented reality technologies, applications and Llimitations *Int. J. Virtual Augmented Real.* **9** 1–20
[2] Peddie J 2017 *Augmented Reality: Where We Will All Live* (Berlin: Springer)
[3] Arthur J, Bailey R, Williams S, Prinzel L, Shelton K, Jones D and Houston V 2017 Review of head-worn displays for the next generation air transportation system *Opt. Eng.* **56** 051405
[4] Liu Z, Pang Y, Pan C and Huang Z 2017 Design of a uniform-illumination binocular waveguide display with diffraction gratings and freeform optics *Opt. Express* **25** 30720–31
[5] Mukawa H, Akutsu K, Matsumura I, Nakano S, Yoshida T, Kuwahara M, Aiki K and Ogawa M 2008 8.4: distinguished paper: a full color eyewear display using holographic planar waveguides *SID Dig. Tech. Papers* **39** 89–92
[6] Xu M and Hua H 2018 Ultrathin optical combiner with microstructure mirrors in augmented reality *Proc. SPIE* **10676** 1067614
[7] Cheng D, Wang Y, Hua H and Talha M M 2009 Design of an optical see-through head-mounted display with a low f-number and large field of view using a freeform prism *Appl. Opt.* **48** 2655–68
[8] Song W, Wang Y, Cheng D and Liu Y 2014 Design of light field head-mounted display *Proc. SPIE* **9293** 92930J
[9] Hua H and Javidi B 2014 A 3D integral imaging optical see-through head-mounted display *Opt. Express* **22** 13484–91
[10] BAE Systems Striker® II digital helmet-mounted display 2020 (available at: www.baesystems.com/en/product/striker-ii-digital-helmet-mounted-display) (Accessed 10 July 2022)
[11] Rockwell Collins F-35 Gen III helmet mounted display system (HMDS) 2022 (available at: www.collinsaerospace.com/what-we-do/industries/military-and-defense/displays-and-controls/airborne/helmet-mounted-displays/f-35-gen-iii-helmet-mounted-display-system) (Accessed 10 July 2022)
[12] Pulli K 2017 11–2: *Invited paper*: meta 2: immersive optical-see-through augmented reality *SID Dig.Tech. Papers* **48** 132–3
[13] Leapmotion Inc Project north star 2018 (available at: http://blog.leapmotion.com/north-star-open-source) (Accessed 10 July 2022)
[14] Mira Labs Mira prism 2022 (available at: www.mirareality.com/hardware) (Accessed 10 July 2022)
[15] Dunn D, Tippets C, Torell K, Kellnhofer P, Akşit K, Didyk P, Myszkowski K, Luebke D and Fuchs H 2017 Wide field of view varifocal near-eye display using see-through deformable membrane mirrors *IEEE Trans. Vis. Comput. Graph.* **23** 1322–31
[16] Akşit K, Lopes W, Kim J, Shirley P and Luebke D 2017 Near-eye varifocal augmented reality display using see-through screens *ACM Trans. Graph.* **36** 1–13
[17] Akşit K, Chakravarthula P, Rathinavel K, Jeong Y, Albert R, Fuchs H and Luebke D 2019 Manufacturing application-driven foveated near-eye displays *IEEE Trans. Vis. Comput. Graph.* **25** 1928–39
[18] Bauer A and Rolland J 2014 Visual space assessment of two all-reflective, freeform, optical see-through head-worn displays *Opt. Express* **22** 13155–63
[19] Koneva T and Romanova G 2018 Designing of a monocular see-through smart glass imaging system *Proc. SPIE* **10676** 106760V
[20] Lanman D and Luebke D 2013 Near-eye light field displays *ACM Trans. Graph.* **32** 1–10
[21] Hong J, Min S and Lee B 2012 Integral floating display systems for augmented reality *Appl. Opt.* **51** 4201–9
[22] Maimone A, Lanman D, Rathinavel K, Keller K, Luebke D and Fuchs H 2014 Pinlight displays: wide field of view augmented reality eyeglasses using defocused point light sources *ACM Trans. Graph.* **33** 1–11
[23] Yao C, Cheng D, Yang T and Wang Y 2018 Design of an optical see-through light-field near-eye display using a discrete lenslet array *Opt. Express* **26** 18292–301
[24] Georgiev T and Lumsdaine A 2009 Depth of field in plenoptic cameras *Proc. Eurographic* (European Association for Computer Graphics) p 4
[25] Bosserman D and Freeman C Toroidal reflector display *U.S. patent 4,026,641 A* (31 May 1977)
[26] Park S, Hoskinson R, Abdollahi H and Stoeber B 2015 Compact near-eye display system using a superlens-based microlens array magnifier *Opt. Express* **23** 30618–33
[27] O'Neill F and Sheridan J 2002 Photoresist reflow method of microlens production part I: background and experiments *Optik* **113** 391–404
[28] Chernov N Circle fit (Pratt method) 2009 (available at: www.mathworks.com/matlabcentral/fileexchange/22643-circle-fit-pratt-method) (Accessed 10 July 2022)
[29] Pratt V 1987 Direct least-squares fitting of algebraic surfaces *ACM SIGGRAPH Comput. Graph.* **21** 145–52
[30] Lin T, Hung S, Hung C, Shen M, Chao C and Yang H 2015 A new fabrication method for an asymmetric microlens array light control film using inclined exposure and an incomplete thermal reflow process *J. Chin. Inst. Eng.* **38** 85–92
[31] Bauer A, Vo S, Parkins K, Rodriguez F, Cakmakci O and Rolland J P 2012 Computational optical distortion correction using a radial basis function-based mapping method *Opt. Express* **20** 14906–20